

High Redshift Candidates and the Nature of Small Galaxies in the Hubble Deep Field

Lisa J. Storrie-Lombardi

SIRTF Science Center, Caltech, MS 220-6, Pasadena, CA 91125; lisa@ipac.caltech.edu

Ray J. Weymann

Observatories of the Carnegie Institution of Washington, 813 Santa Barbara Street, Pasadena, CA 91101; rjw@ociw.edu

and

Rodger I. Thompson

Steward Observatory, The University of Arizona, Tucson, AZ 85721; rthompson@as.arizona.edu

ABSTRACT

We present results on two related topics: 1) A discussion of high redshift candidates ($z > 4.5$) and 2) A study of very small galaxies at intermediate redshifts, both sets being detected in the region of the northern Hubble Deep Field covered by the deep NICMOS observations at 1.6 and 1.1 microns. The high redshift candidates are just those with redshift $z > 4.5$ as given in the recent catalog of Thompson, Weymann and Storrie-Lombardi, while the “small galaxy” sample is defined to be those objects with isophotal area $\leq 0.2''$ and with photometric redshifts $1 \leq z \leq 4.5$.

Of the 19 possible high redshift candidates listed in the Thompson *et al.* catalog, 11 have (nominal) photometric redshifts less than 5.0. Of these, however, only 4 are “robust” in the sense of yielding high redshifts when the fluxes are randomly perturbed with errors comparable to the estimated measuring error in each wave band. For the 8 other objects with nominal photometric redshifts greater than 5.0, one (WFPC2 4–473) has a published spectroscopic redshift. Of the remaining 7, 4 are robust in the sense indicated above. Two of these form

¹Based on observations obtained with the Near-Infrared Camera and Multi-Object Spectrometer and the Wide Field and Planetary Camera 2 on the NASA/ESA Hubble Space Telescope which is operated by AURA Inc., under contract with NASA.

a close pair (NIC 586 and NIC 107). The redshift of the object having formally the highest redshift, at 6.56 (NIC118 = WFPC2 4–601), is problematic, since F606W and F814W flux are clearly present, and the nature of this object poses a dilemma.

Previous work by Colley *et al.* has suggested that compact sources in the WFPC2 HDF images are subgalactic components at redshifts $z > 0.5$ since they are correlated on scales less than $1''$, corresponding to physical scales of less than 8 kpc ($H_0 = 65 \text{ km s}^{-1} \text{ Mpc}^{-1}$, $q_0 = 0.125$). We confirm these correlations in the WFPC2 data. However, we do not detect the correlation of close pairs of galaxies on small scales in the $\sim 0.65''$ region of the HDF that we surveyed with NICMOS. The smaller area surveyed and lower resolution will make any real correlation more difficult to measure in these data. We have examined averaged images of these faint ($V_{606} \sim 27\text{--}29$), compact objects to search for extended, surrounding flux from older, fainter populations of stars. We find no evidence from the averaged images that isolated, compact objects in the Hubble Deep Field are embedded in fainter, more extended galaxies. For three different assumptions about possible star formation histories in these objects we set limits on the total amount of stars which could have been formed in an annulus corresponding to radii between ~ 6 to 10 kpc, which is typically a few times $10^8 M_\odot$. We suggest that some of these objects may be protogalactic fragments.

Subject headings: cosmology: observations – cosmology: early universe – galaxies: formation – galaxies: evolution – galaxies: distances and redshifts

1. Introduction

The redshifts, number counts, sizes, morphologies, and colors of galaxies are used to determine their evolutionary history and constrain cosmological models. It is therefore crucial to understand what we are counting and measuring as we peer deeper into the history of the Universe where objects appear fainter, smaller, and commonly measured features in rest frame optical wavebands move into the near-infrared and beyond. The optical images of the Hubble Deep Field (HDF; Williams *et al.* 1996) showed us an exquisitely detailed view of some high redshift galaxies, though the view is inherently distorted (Ferguson 1998) due to the effects of cosmological surface brightness dimming, the effects of dust on galaxy colors, and the fact that we view higher redshift galaxies at progressively bluer rest wavelengths.

NICMOS observations of the Hubble Deep Field (Thompson *et al.* 1998) provide us with two additional redder wavebands to help disentangle some of these effects. In Thompson,

Weymann, & Storrie-Lombardi (2001; hereafter TWS) we presented a comprehensive table of objects detected in these six wavebands, together with estimates for their redshifts, star-formation rates and internal extinction, and estimated the global star formation rate as a function of redshift based on these results. We also commented briefly on some objects of special interest.

In the present paper, we discuss in more detail two different, but related subsets of objects relevant to the early formation of galaxies: 1) A set of 19 objects which are candidates for being high redshift¹ galaxies according to Table 1 of TWS, regardless of their morphological properties. 2) A set of objects with estimated redshifts at intermediate values, and which are characterized by being very small, some of which may be protogalactic objects which will eventually be assembled into normal galaxies.²

The motivation for examining the high redshift candidates is obvious: We would like to understand the epoch and manner in which the earliest episodes of star formation took place.

The motivation for our study of the set of intermediate redshift, very small objects stems from a paper by (O’Connell & Marcum 1997). For these objects, the combination of the brighter, clumpier star-forming regions moving into the optical filters, and surface brightness dimming will make these intermediate redshift, compact, UV-bright objects more prominent than lower surface brightness objects at the same redshift. (Colley *et al.* 1996) discussed how this is evident in the Hubble Deep Field by measuring the two-point correlation function of galaxies detected in the WFPC2 fields. They found a positive signal in the correlation function for scales ≤ 1 arcseconds for small objects. At cosmological distances this corresponds to subgalactic scales, *e.g.*, 1 arcsecond ≈ 8 kpc for redshifts $z > 1$ ($H_0 = 65$ km s⁻¹ Mpc⁻¹, $q_0 = 0.125$). This led them to suggest that many of the ‘galaxies’ detected by source counting algorithms are probably sub-galactic components. Alternatively, some of these very compact objects could well be small protogalaxies undergoing their first episodes of star formation even though they are at somewhat lower redshifts than the high redshift candidates mentioned above. In this case, some models of galaxy formation suggest that one might *not* expect a strong signal in the two-point correlation on such small scales (Rauch, Haehnelt & Steinmetz 1997 [see pages 603,622]; Steinmetz 1998). Understanding this issue is obviously relevant in how we interpret number counts. The two NICMOS bands enhance our

¹Hereafter we use the phrase “high redshift” to refer to values > 4.5 and the phrase “intermediate redshift” to refer to values $1 \leq z \leq 4.5$.

²For reasons discussed below however, there is not quite an exact one-to-one correspondence between these two subsets and the subsets of objects in TWS meeting similar criteria.

ability to detect fainter, older stellar populations that might be connected with brighter star-forming regions seen at bluer wavelengths, as well as galaxies whose radiation is attenuated by dust at optical wavelengths.

The paper is organized as follows. In § 2 we examine in more detail the list of high redshift galaxies listed in Table 1 of TWS and discuss some of the ambiguities that arise in the interpretation of some of these objects. In § 3 we discuss how the sample of small, intermediate redshift galaxies was selected and the redshift estimates for this sample. In § 4 we discuss averaging the images of fainter galaxies in this sample in order to place limits on the extended flux. In § 5 we discuss the expected extended flux from compact galaxies at intermediate redshifts, based upon moving observed lower redshift star-forming galaxies to higher representative redshifts. In § 6 we examine the two-point autocorrelation function of the optically selected galaxies with high redshift colors and the small galaxies selected in the NICMOS field. In § 7 we summarize and discuss our main conclusions.

2. High Redshift Candidates

Examination of Table 1 of TWS reveals that there are 19 objects whose photometric redshifts exceed 4.5 (Note that because of the lookup table in TWS all the photometric redshifts are quantized in steps of 0.08) In Table 1 we reproduce selected columns of those rows from Table 1 of TWS containing these 19 objects, but now sorted according to the photometric redshifts published in TWS.

Column 1 contains the NICMOS ID number, and, when identification with an object in the Williams *et al.* (1996) catalog has been made according to the precepts given in TWS, column 2 contains the WFPC2 identification. Columns 3,4 contain the total and 0.6 arcsec aperture F160W magnitudes. Columns 5 and 6 are the J2000 coordinates (12h 36m is to be added to the RA; +62 degrees is to be added to the Dec.). Column 7 gives the photometric redshift published in TWS. The remaining columns are explained below. In Figure 1 we show, for these 19 objects, the run of χ^2 vs. redshift for the particular extinction and population template selected by our photometric redshift code. By definition, the lowest value occurs at redshifts above 4.5. However, in some cases it is apparent that there are other minima almost as deep at lower redshifts. The absolute value of the minimum χ^2 fit is not a good indicator of the robustness of the high redshift nature of these candidates, since (cf TWS equation (1)), very faint objects will tend to have smaller values of χ^2 than brighter ones for comparable percentage errors in the fitted and observed fluxes. The relative depth of the primary minimum compared to other minima give some indication of the robustness of the photometric redshift. However, as in TWS, a somewhat better indication of the

robustness of the photometric redshifts can be obtained by randomly perturbing the fluxes according to the estimates for the distribution of the photometric errors in each of the 6 wave bands of interest—F300W, F450W, F606W, F814W, F110W and F160W, though none of these objects have any measurable flux in the F450W or F300W bands. However, in contrast to the “typical” galaxy in TWS, most of these 19 objects are extremely faint, and the photometric errors relatively large. Consequently, the perturbed fluxes yield photometric redshifts which are far less robust than brighter objects. The distribution of these perturbed photometric redshifts is not remotely Gaussian, or even symmetrical about the median value, but typically will have a very low redshift (0 to ~ 1) tail in the distribution of the perturbed photometric redshifts, with a discontinuous jump to high values (typically to $z > 4.0$). For each of the 19 objects in the table, 100 randomly perturbed fluxes were generated and run through exactly the same photometric redshift estimation algorithm described in TWS. For a given object, when these redshifts are ordered, their ranks can thus be crudely regarded as confidence estimates for the redshift. In columns 9 and 10 we give the redshifts at which $\sim 5\%$ of the perturbed set have a lower value, and for which $\sim 10\%$ of the perturbed set have a higher value. In view of the comment above about the discontinuous nature of these redshift distributions, another indicator of robustness is the rank at which the redshift is above 4.0, and this rank is given in column 11. In the discussion below we consider that if this rank is 5 or less (ie, less than 5% of the perturbed redshifts fell below 4.0) then the classification of the object as a high redshift galaxy is “robust”. In column 8 the symbol R is used for the robust objects and NR for the non-robust objects. We now give a very brief description of the morphology and run of the χ^2 fit with redshift for each of the robust objects, and, because of its peculiar nature the object with the highest nominal photometric redshift in the TWS list, NIC118.0.

NIC131.0:

There is a well-defined minimum at the published photometric redshift; all the other secondary minima are much poorer fits. It is a very faint smudge on the F606W image, distinctly brighter and resolved on the F814W image with an indication of a brighter nucleus. Both the F110W and F160W images are slightly resolved and readily visible, though the lower resolution of the NICMOS images prevents detailed comparison between the F110W and F160W images and the WFPC2 F606W and F814W images, a comment that applies to all subsequent objects and will not be repeated.

NIC274.0:

While there is a well-defined minimum at $z = 4.64$, a secondary minimum at a redshift of 0.80 is almost as deep, and is fit by a hot unreddened population, whereas the fit at 4.64 requires some reddening of a hot population. Thus, while this is formally robust against flux perturbations, its reality as a high redshift object is less convincing than for NIC131.0. The

F606W image appears compact, while the F814W image appears to have a small extension. The F110W image is bright with no obvious structure, while the F160W image shows a small nearby companion.

NIC267.0:

A well-defined minimum occurs at $z = 4.80$, and there is no other reasonable fit. All four images are compact and show no structure.

NIC150.0:

As in NIC267, the χ^2 plot against redshift shows only a deep minimum at a redshift of 4.80 and no other reasonable fit. There is no WFPC identification and no object is visible on the F606W image. However there are two small slightly amorphous objects clearly visible on the F814W image, one of which agrees well with the nominal F160W and F110W coordinates. However both the F110W and F160W images show the same two small objects with possibly a more diffuse fainter chain-like structure underlying them.

NIC277.212:

The primary minimum at a redshift of 5.04 is deep, but rather broad. There is also a well defined secondary minimum at a redshift of 0.8, though not nearly as good a fit as the high redshift minimum. The F160W image does not separate this object from a nearby larger and brighter galaxy, but the F110W image shows it as an apparently well-separated object. The WFPC2 images are curious, in that the F814W image is quite bright, but there is no convincing evidence at all of the object in the F606W image, which, given the brightness in the F814W image and the nominal redshift is surprising. Thus, the nature and redshift of this object is somewhat suspect.

NIC184.0 = WFPC2 4–473.0:

This object has a spectroscopically determined redshift of 5.60 and was the subject of a separate publication (Weymann *et al.* 1998), and will not be discussed further here.

NIC645.0:

A well-defined minimum exists at a redshift of 5.52, and there is no reasonable secondary minimum. This is an extremely faint object, barely discernible in both F110W and F160W and somewhat diffuse in F110W. The F814W image is readily apparent and slightly elongated, (and hence has a WFPC2 identification), although there is no convincing evidence for flux in the F606W image. In this respect this object is somewhat similar to NIC184.0, (which has the same photometric redshift).

NIC586.0 and NIC107.0:

We consider these two objects together since they are separated by only about 1.0 arcsec. Both objects are extremely faint. The deepest minimum for NIC586.0 yields the photometric

redshift of 5.68, but the minimum is not very well defined nor is the fit very good. The same remarks apply to the χ^2 curve vs. redshift for NIC107.0, whose deepest minimum yields a photometric redshift of 5.92. The F160W image of this pair shows one compact and one slightly diffuse object in a field with several other nearby objects. There appears to be no doubt about the reality of these two objects on the basis of the F160W image. However, the flatfield properties of the F110W image in this area of the chip are rather grainy and noisy and it is difficult to compare the morphology of the two images, and the F110W photometry is quite uncertain. There is a barely discernible very compact object in the F814W image at the appropriate position for NIC586.0, but nothing visible for NIC107.0. No convincing evidence for either object appears in the V image.

NIC118.0 = WFPC2 4–601.0:

This object was discussed in TWS. It is not a robust object in the sense described above, but we discuss it because it has the highest photometric redshift in the TWS table and because its interpretation is not at all clear.

Our measured 0.6" AB magnitudes for the F160W, F110W, F814W, and F606W wavebands are 27.79, 27.68, 30.41 and 30.44. In a qualitative way, this might be thought consistent with a high redshift, and our formal fit has a fairly well defined minimum at the photometric redshift of 6.56. However at the photometric redshift given in TWS, it is difficult to understand how there could be any flux whatsoever in the F606W band. The significance of the V_{606} and I_{814} detections in our convolved images is only about 1σ but in the original WFPC2 images this object is detected with a 5.75σ significance. Visual inspection of the images makes it almost certain that there are positive detections in the V_{606} and I_{814} wavebands and that the V_{606} flux is not substantially less than the I_{814} flux (see discussion and figure in the appendix).

Alternatively, the object might be a lower redshift, but highly reddened object. A second alternative involves the chance superposition of two objects of quite different redshifts. None of these interpretations is at all satisfactory, as discussed in some detail in the Appendix.

We close the discussion on high redshift candidates by comparing our photometric redshifts of the 19 objects with redshifts ≥ 4.5 with the only other extensive compilation which extends to high redshifts in our field, namely the catalog of Fernandez-Soto *et al.* (1999), hereafter FLY. These authors provide a list of 170 photometric redshifts which fall in our deep NICMOS field on chip 4, which is to be compared with the list of 282 in TWS. FLY based their photometric redshift estimates on the 4 WFPC2 bands augmented by ground-based observations in the standard J, H, and K bandpasses. These ground-based observations have, of course, much lower spatial resolution than the NICMOS images, and the J and H observations do not go nearly as deep as the F110W and F160W NICMOS fluxes. Consequently,

for the very faint objects on our list, these ground based observations generally do not yield statistically significant detections. Nevertheless it is of interest to compare the results from the two catalogs.

As explained in TWS we cannot make unique associations in all cases with objects from the two lists because of differences in the weight given to different bandpasses in composing the detection images, and in the parameters used by SExtractor in breaking up significant pixels into separate objects. Nevertheless, if we examine the histogram formed by looking at the distance between each object in the list of each of the 170 objects in FLY to the nearest object in the TWS catalog, there is a large cluster of objects with agreement in coordinates less than $0.15''$ whose median value is about $0.05''$. There are 155 such objects. Of the remaining 15, all but one are either so near the boundary that we rejected it from our list of 282 objects, or else they fall within the boundaries of a clump of pixels which, for our SExtractor parameters applied to our images, are treated as part of a nearby object. Evidently there are 127 objects in the TWS list which have no clear association with an object for which FLY give a photometric redshift, though in many cases the objects are obviously present but apparently too faint, given the data available to FLY, to derive photometric redshifts.

If we confine ourselves to objects in any one of these three lists with redshift of 4.5 or greater, then of the list of 15 FLY objects which have no TWS unambiguous identification, there is one object (FLY #393) which has a photometric redshift of 4.56. On the F160W image it appears as an appendage on the very large low redshift galaxy NIC 26.100 and was not separated with our SExtractor parameters. However, on the V and I images it appears cleanly separated and is almost certainly a separate object. In the list of 127 objects in the TWS catalog not appearing in the FLY catalog there are 13 out of our high redshift list of 19, so there is no basis for comparison among these objects: NIC #s 108, 1075, 150, 92, 693, 562, 96, 1040, 645, 586, 248, 107, and unfortunately, 118 = WFPC2 4–601 the object discussed at length in the Appendix. Finally, among the 155 objects which can be unambiguously associated in both catalogs, there are two in the FLY catalog which do not appear in our list of 19 high redshift candidates: NIC 103 (WFPC2 4–625.1) and NIC 1062.0 (WFPC2 4–600.0 = FLY 471), however in both cases the TWS redshift is just below our cutoff with photometric redshifts of 4.48, compared to 4.52 given in FLY for NIC 103 and 6.52 for NIC 1062.0. We return to NIC 1062.0 below.

Our high redshift list contains two objects for one of which the discrepancy between FLY and TWS is mild (NIC 131 = WFPC2 4–530 where TWS obtain $z = 4.56$ and FLY obtain $z = 4.32$) and one serious discrepancy (the non-Robust object NIC 287 = WFPC2 4–148.0 where TWS obtain 4.64 and FLY obtain 1.24).

In the case of NIC 287 = WFPC2 4–148.0 = FLY#305, our fluxes give a much better fit at $z = 4.64$ than at 1.24 in all three colors (V-I), (I-J), and (J-H).

The image of NIC 1062 = WFPC2 4–600 is very curious. It lies about 0.7 arcsec from a much brighter object, NIC61. It is most prominent in the F814W image, where it appears as a somewhat diffuse object with only moderate central concentration. The F606W image is very much weaker and the SNR is much lower than in the F814W image, and its flux will depend upon exactly which pixels are included in the measurement. FLY used the F814W profile as a template for the aperture in which all the other bands were measured, and obtained an AB V-I color of about 2.77—this is presumably what drove their very high redshift value of 6.52

The NICMOS F160W and F110W images are unexpectedly weak, and the contamination from NIC61 appears to be more severe than in the F606W and F814W bands. This makes the flux measurements in the two NICMOS bands problematic. While in principle we might attempt to deblend the NIC1062 and NIC61 images, the SNR of NIC1062 is not high enough in the two NICMOS bands to make this practical. There were 12 pixels in the original “detection map” used in TWS for the NIC1062 fluxes. In an attempt to minimize the contamination from NIC61, we dropped three pixels between NIC61 and NIC1062 and remeasured the fluxes with SExtractor. For these measurements we used only the flux contained within a 3x3 pixel square centered on the coordinates of NIC1062 in the F814W image rather than the 0.6” aperture fluxes of TWS. Even in this case however, the F160W flux and especially the F110W flux may suffer from significant contamination by NIC61.

Nevertheless, taking at face value these new flux measurements we still obtain virtually the same redshift for NIC1062 (4.64) compared with that given in TWS (4.48). The fit obtained predicts a flux in the F110W band which is about twice that observed, but the SNR in this band is only about one so the discrepancy is not necessarily indicative of a failure in the template.

On the other hand, the very high redshift of order 6.5 obtained by FLY seems very unlikely: Our best fit at this redshift to the fluxes measured in the 3x3 patch predicts an F814W flux which is nearly 7 sigma lower than the observed value. The situation is even worse if, as suggested above, we have overestimated the F160W and F110W fluxes because of the contamination from NIC61.

In summary, the detection of 9 robust high redshift candidates with five candidates at redshifts greater than 5 in an area of less than 1.0^{\square} indicates that adding the near infrared bands to the deep optical images is an excellent way to identify high redshift objects. The flux measurements in the F160W band essentially double the range of identification of

high redshift galaxies via the strong Lyman break. It is clear from Fig. 4 of TWS that these galaxies are at or near L^* luminosities, indicating that such luminosities exist at high redshifts where the hierarchical models expect very few high mass galaxies. However, since these galaxies have SEDs that are dominated by very high mass, extremely luminous stars, high luminosity does not necessarily imply high mass. In the next section we examine the question of small galaxies at intermediate redshifts.

3. Selecting Compact, Intermediate Redshift Galaxies

As noted in the introduction, an exact one-to-one correspondence does not exist between the list of objects presented in this section and that which would result from a similarly selected subset of objects in Table 1 of TWS. As explained in TWS the selection of objects for inclusion in that paper was based upon a “ χ^2 ” map following the prescription of Szalay, Connolly, and Szokoly (1999). There, since we had a particular interest in identifying objects to the highest possible redshift, we used only the equally weighted F814W, F110W, and F160W wavebands in composing the χ^2 map. For the present purpose, at the low end of the intermediate redshift regime in which we are interested, there will be important information in both the F450W and F606W WFPC2 images, and hence we used a χ^2 map based upon equal weights for the F450W, F606W, F814W, F110W, and F160W wavebands. However, we used the same significance level to define “significant pixels” (2.3) and the same required minimum number of contiguous pixels (3) in the SExtractor algorithm (Bertin & Arnouts 1996) as used in TWS. Since most of these very small objects are at the very edge of our detection threshold, we elected to measure “isophotal” fluxes (or, more precisely, the flux contained in all the “significant” pixels as defined in the χ^2 map) rather than fluxes measured through an 0.6 arcsecond aperture, in order to keep sky noise to a minimum. Otherwise, the methodology for selection, flux measurement, flux error estimation, the estimates for the photometric redshift, template type and internal extinction as well as their attendant errors, are exactly as described in TWS. The higher resolution images were convolved to match the F160W images. The goal was to select galaxies that are centrally concentrated as well as those where we are only detecting a bright knot measured above our detection threshold.

For our sample of compact objects, we then selected a subset of the objects detected by SExtractor with the parameters described above, using the following criteria:

- The “isophotal” area, as measured by SExtractor on the χ^2 map, is $\leq 0.2^{\square}$.
- The photometric redshift is $1.0 \leq z \leq 4.5$.

- The SExtractor parameter `FLAGS=0` was required, so we only select objects that are not blended/overlapping with others and are not on the edge of the image.

This resulted in 93 selected galaxies.

As in TWS we tested the robustness of the photometric redshifts determined for this sample by perturbing the fluxes in each of the 6 wavebands, and then running the perturbed fluxes through the photometric redshift estimator.

This set of small compact objects tends to be at least as faint as the high redshift candidates in the previous section, so that once again the photometric errors are large and the resultant uncertainties in the estimated photometric redshifts are very large. In fact, of the 93 galaxies in our sample, only 11 have percentile values z_{10} and z_{90} within $\Delta z = 0.5$ of the value determined from the unperturbed fluxes.

4. Averaging Images to Place Limits on Extended Flux

The 11 robust galaxies identified in the previous section may be separated into three groups: (i) Those with detectable F300W flux with photometric redshifts less than ~ 2.0 , of which there are two. (ii) Those with detectable F450W flux but little or no detectable F300W flux, whose photometric redshifts cluster around $z \sim 2.7$, of which there are six. (iii) Three additional objects with little or no detectable flux in either F300W or F450W whose redshifts are around $z \sim 3.9$. Groups (ii) and (iii) we refer to as “F300W dropouts” and “F450W dropouts”.

For the remaining 82 galaxies, the photometric uncertainties are too large at these faint flux levels to obtain individual reliable photometric redshift estimates. Instead, we simply visually inspected the images in all six wavebands and placed them into one of the three categories above. Even though these are faint objects the quality of the HST images and the availability of six wavebands makes grouping them into categories with and without F300W/F450W flux very straightforward. While this procedure certainly does not provide an accurate redshift discriminant it should provide a rough guide to the redshift range appropriate for these three groups.

From the two groups of F300W and F450W dropout galaxies thus assembled we next selected those which appeared to be “truly small”. This was done by visual inspection of the images, keeping only those which have no close companions and show no obvious extended flux.

The objection might be raised that this is a circular procedure, in which by selecting

objects showing no extended flux we find objects with no extended flux! But our objective is to discover whether there is *any* subset of the small galaxies which show no extended flux. This procedure resulted in 14 “isolated F450W dropouts” and 23 “isolated F300W drop” galaxies. Only two of the galaxies with robust photometric redshifts are included in this subsample. We then averaged together each waveband at the galaxy positions and used the fluxes measured from these images to obtain a ‘mean’ photometric redshift for each ‘averaged’ F300W drop and F450W dropout galaxy. The F300W dropout mean redshift is in fact $z = 2.7$ and the F450W dropout mean redshift is $z = 3.9$. In both cases the hottest galaxy template (a 50 Myr starburst; template #6 in TWS) with a small amount of reddening is preferred. Images for all six HST wavebands for the (averaged) F300W and F450W dropouts are shown in Figure 2. Overplotted are 1.0 arcsecond diameter apertures. The galaxies still appear compact in the averaged images. The galaxies in the averaged samples have similar fluxes but we were concerned that the brightest galaxies might dominate the average. We did experiments removing the brightest one or two galaxies from the stack but this didn’t change the results.

Since we expect any older stellar population surrounding the small nucleus to be redder than the population comprising the nucleus itself, one check for the existence of such an older population is to measure the colors of the galaxies in successively larger apertures. Within the uncertainties they are constant (Table 2). It is difficult to get accurate photometry at these faint magnitudes so we measured the colors with both the SExtractor and IRAF photometry routines. These give consistent results. The errors calculated for the photometry are of order ± 0.1 . It can be seen from the table that the uncertainties are at least this large as the 2.5” aperture gives a slightly fainter magnitude than the 1.5” aperture for the F160W filter.

There is no evidence for diffuse, redder flux outside of the core. The F160W images for these “averaged” galaxies were remeasured with SExtractor and yield isophotal diameters of $\sim 0.5''$, which corresponds to $\sim 4kpc$ ($H_0 = 65 \text{ km s}^{-1} \text{ Mpc}^{-1}$, $q_0 = 0.125$). If we measure the 3σ limiting depth in the blank sky at 1.6 microns in a 1.5” – 2.5” diameter annulus we obtain an F160W AB magnitude of 29.3 for the F300W dropout and 29.4 for the F450W dropout. Limits on the amount of previous star formation that we can infer from these limits are discussed in § 5.2.

5. The Expected Extended Flux from Compact Galaxies

In § 4 we set approximate empirical limits on the count rate in the F160W band through an annulus with inner diameter 1.5” and outer diameter of 2.5” associated with the mean

of the isolated F300W and F450W dropout galaxies described above. Our failure to detect such extended flux may be interpreted in at least two ways:

1. They are either the bright nuclei or star-forming knots in galaxies with significantly lower average surface brightness made up of an older, cooler population (we make no attempt to distinguish between these two possibilities).
2. They are young protogalaxy fragments which are not embedded in an older stellar population.

Colley *et al.* (1996) argue for the former of these two possibilities on the basis of the two-point correlation function, but our sample from the NICMOS field contains too few objects to make this a decisive test (see § 6).

When we repeat the Colley *et al.* analysis on the HDF north WFPC2 chips 2,3 and 4 optical data set (see § 6) we also find a significant signal in the autocorrelation function on small scales, but visual inspection of the images shows that the galaxy pairs responsible for the signal are often obviously two pieces of the same galaxy. Clearly, in such cases, the Colley *et al.* interpretation of compact “galaxies” is the correct one.

5.1. Simulating Extended, Old Stellar Populations

Alternatively, we can ask whether surrounding lower surface brightness material from a putative older population would be expected to be detectable or not if it were placed at either of the two representative redshifts ($z = 2.7$ and $z = 3.9$) inferred for the F300W and F450W dropout subsamples described above, and what the limits are for the stellar mass of an extended older population. For illustrative purposes, and to stay as close as possible to the data set we are analyzing, we selected a relatively bright galaxy from the HDF, WFPC2 4–378 (Williams *et al.* 1996), with a photometric redshift of $z = 1.20$ (NIC 124.000 and 1022.00, TWS; the redshift has since been measured spectroscopically at $z=1.225$ by Cohen *et al.* 2000.)

This object provides a good example of a galaxy with bright star-forming regions surrounded by an older population or less actively star-forming regions. To test the robustness of the photometric redshift estimate with respect to where in this galaxy the flux is measured we selected 4 different aperture positions: 1=bright F160W nucleus, 2=bright F814W off-nuclear knot, 3=dim F814W off-nuclear region, and 4=the whole galaxy. The flux was measured in 0.6” diameter apertures for positions 1 through 3 and a 2.6” aperture for position 4. These are marked on the F606W+F814W image shown in figure 3. It has been

scaled and rotated to match the NICMOS orientation and resolution and the image stretch has been set to emphasize the lumpy nature of the morphology. The F606W–F160W colors range from 1.91 for position 1 to 0.86 for position 4. The photometric redshifts for each of these apertures were $z = 1.20$ or $z = 1.25$.

We then measured the flux in an 0.6–1.5 arcsecond annulus centered on the bright nucleus. This is the region we would hope to detect at higher redshift if the compact galaxies in our sample are embedded in a comparable extended source. The best least squares fit between the observed broadband *annular* fluxes and those calculated on a grid of models in redshift–reddening–population type space for this galaxy is very good and constrains the spectral energy distribution over the range covered from the F300W band to the F160W band fairly tightly (even though there is ambiguity between, *e.g.*, a very hot, but internally reddened population and a somewhat cooler but unreddened population, c.f. the discussion in § 6.3 of TWS). With this best fit model, and the observed flux in the bandpasses which most nearly correspond to the 1.6 micron bandpass if the $z = 1.225$ galaxy were redshifted to $z = 2.7$ or $z = 3.9$, we can calculate the expected flux at higher redshift. (In this calculation we ignore the change in proper length with fixed angle, since over this redshift range this change is very small for most cosmological models.)

Figure 4 simulates what we would expect to see if our F300W and F450W dropout galaxies were embedded in WFPC2 4–378.0 at a redshift of $z = 2.7$ or $z = 3.9$ and were observed at 1.6 microns. The redshift $z = 2.7$ case is on the left and the $z = 3.9$ case is on the right in the figure. The top panels again show the averaged dropout galaxies at F160W. The center panel shows how WFPC2 4–378.0 would look at 1.6 microns when scaled to the expected brightness at $z = 2.7$ and $z = 3.9$. The circles overlaid on the images are 1 arcsecond in diameter. To create the simulated higher redshift images we used the photometric redshift SED template that best fit the measured fluxes of the galaxy at $z = 1.225$ and calculated what we would detect in the F160W bandpass for this galaxy at if it were at $z = 2.7$ or $z = 3.9$. We ignored any changes in angular size as the angular size relation is roughly flat for $z > 1$. We dimmed the F606W+F814W image shown in figure 3 appropriately and added this and added this to blank ‘sky’ regions from the full NICMOS F160W image that have been averaged together. The bottom panels were created by adding the dimmed versions of 4–378.0 to the dropout galaxies shown in the top panels. Though the full extent of 4–378.0 would not be visible at either $z = 2.7$ or $z = 3.9$, comparison of the top and bottom panels makes it obvious that the resulting simulated version of WFPC2 4–378 at these higher redshifts is larger than the isolated galaxies we have detected, and the flux is readily measurable outside of a 0.6” aperture.

In § 4 we made averaged images that were centered on the compact source in each field.

If the objects in our sample are truly off-nuclear star-forming knots in an underlying star-forming galaxy, then to make a simulation that more accurately mimics what these averaged images might contain, we have again taken the galaxy WFPC2 4–378.0 and randomly rotated the galaxy around 2 different bright knots, marked **A** and **B** in figure 5 which shows the same image as figure 3. We then take 20 of the randomly rotated galaxies and average these together in the same way we made the F300W and F450W averaged dropout galaxy images. The result is illustrated in figure 6.

Both of these ‘averaged’ galaxies now show much more diffuse morphology. (Note that though WFPC2 4–378.0 has a bright nucleus in the F160W band, it is not apparent in the F606W and F814W images. Therefore when we make the dimmed, averaged images for $z=2.7$ and $z=3.9$ centered on the off-nuclear knots using the HDF optical images, we are not smearing a bright nucleus into appearing as extended flux.) The results from adding these simulated galaxies to the F300W dropout galaxy and F450W dropout galaxy give a result very similar to what we saw in figure 4.

At $z = 2.7$ the diffuse flux is easily detected by eye in the images. At $z = 3.9$ it is much less obvious. However, when the magnitudes are measured in successively larger apertures, the extended flux is definitely measurable. In Table 2 we showed that the F160W magnitudes for the F300W dropout and F450W dropout galaxies didn’t change when measured in 0.6”, 1.5”, and 2.5” apertures. After adding the simulated, extended galaxies to these images, the F300W dropout galaxy ($z = 2.7$) is ~ 0.4 mags brighter in the 1.5” aperture and ~ 0.9 mags brighter in the 2.5” aperture in both the knot-A and knot-B cases. The B-drop galaxy ($z = 3.9$) is ~ 0.9 mags brighter in the 1.5” aperture and ~ 1.5 mags brighter in the 2.5” aperture. Though faint, the flux from the extended galaxies is detected over an extent of 2 arcseconds. If the compact galaxies we have estimated to be at redshifts $z > 1$ were embedded in more diffuse, larger galaxies, such as WFPC2 4–378, we would be able to measure this extended flux in the NICMOS images.

5.2. Limits on The Star Formation History of the F300W and F450W Dropout Galaxies

While the foregoing examples suggest that significant star formation occurring outside the nucleus of distant galaxies, similar in character to WFPC2 4–378 would be detectable in our averaged dropout galaxies, we now address the more quantitative question of limits on star forming activity in these dropout galaxies.

In § 4 we measured the 3σ upper limit on the flux in the F160W filter in an annulus of

1.5" – 2.5" diameter for the averaged F300W dropout and F450W dropout galaxies. These measurements give $F160W=29.3$ for the F300W dropout and $F160W=29.4$ for the F450W dropout. This annulus corresponds to an inner and outer radius of about 6 and 10 kpc, respectively—an annulus centered roughly on a strip whose center is comparable to the sun’s galactocentric distance. We now investigate what limits on the star formation history in this region the flux limits imply for these two averaged galaxies.

In the following we consider models for star formation which commenced at about $z \approx 6.0$ Although we have referred previously to a possible underlying “old” stellar population, the intervals of time between the epochs corresponding to $z \approx 6.0$ and $z=2.7$ (for the F300W dropouts) and $z \approx 6.0$ and $z = 3.9$ (for the F450W dropouts) are only about 1.4 and 0.6 Gyrs, respectively, so that we would expect an intermediate age, rather than old stellar population to be present.

Out of the infinite number of possible star formation histories, we consider three:

(i) An initial burst of star formation of duration 50my which began at a redshift slightly less than 6.3 and ended at a redshift of 6.0 (ii) An intermediate case in which star formation began at $z = 6.0$, decayed exponentially with a time constant of 1 Gyr, but with a constant amount subtracted from this exponentially decaying star formation rate, so that at the epoch of observation the star formation rate had reached zero. (iii) A burst of star formation of duration 50mY which ended just at the epoch of observation. The models include dust extinction using the procedure described in TWS, section 3.2. The best fit includes a small amount of extinction. The results are shown in table 3. The three rows represent cases (i), (ii) and (iii) while columns 2 and 4 give the total mass of stars formed over the observed annulus which would just produce the observed 3σ limit on the F160W flux in the annulus. Columns 3 and 5 give the corresponding instantaneous rates of star formation (in solar masses per year) for case (iii).

In the rest frame of objects at $z = 2.7$ and $z = 3.9$, the center of the F160W band pass at 1.6 microns occurs at 4324 and 3265 Å respectively. The limit for the F300W dropout at $z = 2.7$ is of course considerably more stringent, simply by virtue of being closer than the F450W dropout. For case (i), which postulates a single initial brief burst of star formation at $z = 6.0$, occurring anywhere in the outer annulus, the hottest stars have left the main sequence. For the F300W dropout case the F160W band flux samples the region just longward of the Balmer discontinuity and a spectrum would show strong Balmer lines from an intermediate age population. For the intermediate case (ii) the SED is qualitatively similar, but a more extended period of star formation implies that the limit on the total mass of stars formed is significantly less. Case (iii) does not refer to an older population, but merely says that the star formation responsible for the images actually seen in the HDF was confined to a

small region, and very little could have occurred in the surrounding annulus. The situation for the F450W dropouts is qualitatively similar, except that in addition to the fainter flux as a consequence of the greater distance, the F160W band for this redshift samples rest wavelengths which are shortward of a strong Balmer discontinuity, though in case (ii), the interval of time between the start of the star formation at a redshift of 6 and the epoch corresponding to the redshift of $z = 3.9$ is smaller than the decay time, and consequently there is still significant flux from fairly hot stars.

6. Spatial Galaxy Correlations

6.1. Galaxies Selected from WFPC2 Data

We examine here the scale on which the galaxies are correlated in the WFPC2 fields to compare with the results of Colley *et al.* (1996). They found a positive signal in the correlation function on scales ≤ 1 arcsecond for high and low redshift color cuts. In particular, they found that for the smallest objects, as well as those with colors that suggest they are at redshifts $z > 2.5$, there is a strong autocorrelation for scales ≤ 0.5 arcseconds. The color cut used was $F300W - F450W > 1.2 + F450W - (F814W + F606W)/2$ (Steidel *et al.* 1996).

As an estimator for the two-point angular correlation function, $w(r)$, we used

$$w(r) = \frac{N_{dd}(r)}{N_{dr}(r)} \frac{2n_r}{(n_d - 1)} - 1 \quad (1)$$

(Efstathiou *et al.* 1991; Roche *et al.* 1996), where N_{dd} is the number of pairs in our data set, N_{dr} is the number of pairs in n_r randomly placed objects in our field, and n_d is the number of objects in our data set. We calculated $w(r)$ in 0.25 arcsecond bins out to a radius of 5.0 arcseconds with $n_r = 10,000$.

We extracted galaxies from combined F606W + F814W images of the WFPC2 chips 2, 3, and 4 HDF north fields with SExtractor (2.5σ threshold, 10 pixel minimum area). We next selected a catalog of galaxies matching the above color criterion from $71.0'' \times 69.2''$ central regions of the chips that miss the lower signal-to-noise regions near the edges. This results in 273, 215, and 222 galaxies from chips 2, 3, and 4 respectively. The results for the autocorrelation function of this high redshift sample are shown in figure 7. The data are plotted as stars (WF2), triangles (WF3), and circles (WF4). The $\pm 1\sigma$ range for no correlation, determined from 500 realizations of 10000 randomly placed points, is shown as the crosshatched region around $w(r) = 0$. The high redshift color sample has a strong signal for all three WFPC2 chips on scales less than $0.5''$, confirming the result found by Colley *et al.* (1996). The signal is significant at the $3 - 7\sigma$ level, and peaks at $0.25'' - 0.5''$. No

significant autocorrelation is seen at separations $> 1''$. When we examine the pairs on the F606W image, it is clear that SExtractor has counted 2 pieces of what appear to be the same galaxy in many of these cases. Two examples of this are WFPC2 4-603.0 (NIC110.000) and WFPC2 4-555.1 (NIC141.112), also known as the “hot dog”. Their respective redshifts are $z=2.56$ (photometric, TWS) and $z=2.803$ (spectroscopic, Steidel *et al.* 1996).

6.2. Galaxies Selected from NICMOS Data

We ran the same analysis discussed in the previous section on our catalog of 93 small galaxies from the NICMOS data set. To determine the uncertainty we ran the same estimator on 500 sets of 93 randomly placed galaxies. The results are shown in figure 8. In contrast to the results discussed above for the WFPC2 data, we see no correlation signal in the NICMOS data.

It is difficult to interpret whether this result means that (a) the small objects are not correlated, or (b) the lower resolution in the NICMOS image compared to the WFPC2 data and/or our smaller survey region preclude measuring any signal above that expected from random superpositions. In the near-infrared many galaxies will appear smoother since we are observing older stellar populations and SExtractor will be less likely to break them into multiple pieces. To determine how the correlation signal would be affected by examining a smaller region of the sky, we then reran the analysis of the WFPC2 color-selected catalog, but just used the data from $0.65''$ regions in each chip, the areal size covered by our NICMOS observations. The results are shown in figure 9.

Using the smaller region the correlation signal is stronger in WF4, about the same in WF2, and has disappeared in WF3 when compared to the full area measurements shown in figure 7. Our $0.65''$ region may hinder the detection of a real signal with these faint objects, but it may also be that our small galaxies constitute a set of objects with genuinely different correlation properties than the set defined in the Colley *et al.* (1996) analysis. Thus, we can neither confirm nor reject the hypothesis that the 93 small galaxies from the NICMOS data set are uncorrelated.

In summary, we confirm the Colley *et al.* (1996) result finding a positive signal in the autocorrelation function on scales ≤ 1 arcsecond for objects detected in the WFPC2 images with colors suggesting they are at high redshift. We do not detect any significant signal in the autocorrelation function for the small, moderate to high redshift galaxies detected in the NICMOS image. However, we cannot make a decisive interpretation of this due to the small size of our sample.

6.3. Correlation of Blue and Red Galaxies

It was apparent just by looking at the optical and infrared images that there were a number of cases where faint blue smudges were next to brighter red galaxies but were not obviously pieces of the same galaxy. An example is shown in figure 10. The left panel shows a $4.5'' \times 4.5''$ WFPC2 F606W image and the right panel shows the same region through the F160W filter. The galaxy just left of the center in both images is WFPC2 4–307.0 (NIC166.000). WFPC2 4–312.0 is the galaxy $1.5''$ to the right of WFPC2 4–307.0 and WFPC2 4–279.0 is the galaxy $2.1''$ above 4–307.0 in the F606W image. The two blue objects, WFPC2 4–312.0 and WFPC2 4–279.0, were not formally detected by SExtractor using the S/N thresholds we have adopted and thus do not have NICMOS identifications. However, measuring the F160W flux at the centroids expected yields AB F606W - F160W color indices of ≤ -0.3 and ≤ -1.0 respectively. Conversely, WFPC2 4–307.0 is one of the brighter objects in the NICMOS catalog and yields a color index of $+4.2$. (See the figure caption for details). We estimate a photometric redshift of $z \approx 1.85$ for WFPC2 4–307.0. Though WFPC2 4–312.0 and 4–279.0 could be galaxies unrelated to WFPC2 4–307.0, their proximity and color are also consistent with star-forming regions 12–16 kpc from the center of WFPC2 4–307.0.

Pairs of red and blue galaxies such as these motivated us to look for a statistical correlation between the very blue and redder populations. Similar to the autocorrelation analysis described above, we measured the separations of blue and red galaxies with respect to what we might see with randomly placed samples in our region. We selected samples of galaxies with ‘blue’ ($F606W - F160W \leq 0.3$) and ‘red’ ($F606W - F160W \geq 1$) colors then measured the separations of all the pairs. Here we might have expected to see more pairs at separations of 1–2 arcseconds but no significant signal is detected. As in the autocorrelation analysis though, we cannot use this to completely rule out correlations that seemed apparent when examining the images by eye due to the very small region surveyed.

7. Discussion and Summary: Small Galaxies

We examined averaged images of faint (F606W magnitudes ~ 27 – 29), compact objects to search for extended, surrounding flux from older, fainter populations of stars. We also simulated what extended galaxies, easily detected at $z \sim 1$, would look like at higher redshifts when measured in the infrared wavebands. We have determined that though these galaxies would of course appear substantially fainter, the more diffuse parts of the galaxies would still be clearly detected. Our results suggest that at least some of the small, (isophotal area $\leq 0.2''^2$), high redshift, ($1 \leq z \leq 4.5$), galaxies detected in the HDF are bonafide

compact objects, not bright nuclei or star-forming knots embedded in more extended stellar populations. The limits on the flux in an annulus between 1.5 and 2.5 arcsec in diameter correspond to limits on the total mass of stars which could have been formed in this annulus of a few times $10^8 M_\odot$ for the U-drop galaxies and slightly more for the B-drop galaxies, the exact mass limit depending upon the star formation history assumed. Our simulations have shown that a prototypical extended galaxy with bright clumps detected easily in the HDF at redshift $z \sim 1$ (specifically WFPC2 4–378) would still be detected at $z = 3.9$ in the NICMOS observations at 1.6 microns. This object has had substantial star formation extending to a radius of ~ 10 kpc. In contrast, the objects forming our averaged U-drop and B-drop images are consistent with being young protogalaxy fragments. Our photometric redshift estimator prefers the hottest galaxy template (a 50 Myr starburst) with a small amount of reddening for both the F300W and F450W dropouts, and gives mean redshifts of $z = 2.7$ and $z = 3.9$ for these, respectively.

It has been suggested in previous work (e.g. Colley *et al.*) that compact sources in the WFPC2 HDF images are subgalactic components at redshifts $z > 0.5$ since they are correlated on scales less than $1''$, corresponding to physical scales of less than 8 kpc ($H_0 = 65 \text{ km s}^{-1} \text{ Mpc}^{-1}$, $q_0 = 0.125$). Using the data from all the WFPC2 chips we confirm these correlations in objects selected from the optical images with high redshift colors. However, we do not detect the correlation of close pairs of galaxies on small scales in the $\sim 0.65''$ region of the HDF that we surveyed with NICMOS. This is likely due to one or more of the following factors: 1) The area we surveyed with NICMOS is substantially smaller than that covered by the WFPC2 observations. When we sample $0.65''$ regions of the WFPC2 images, where the correlation is found at a statistically significant level in all three WF chips, we no longer detect any correlation signal in the WF3 chip, simply due to the smaller area surveyed. 2) The resolution in the NICMOS images is slightly lower than the WFPC2 images, and in the near-infrared many galaxies will appear smoother since we are observing older stellar populations and they will be less likely to be broken up into multiple pieces by the galaxy detection algorithm. 3) Our selection criteria for small galaxies has yielded a set of objects whose correlation properties are in fact different from those selected by Colley *et al.*.

When we visually examine examples of correlated pairs, many are clearly pieces of one galaxy. Thus, the distinction between “separate correlated galaxies” and patches of the same galaxy is rather artificial and depends not only on the signal-to-noise ratio of the data but also the parameters used in the source extraction algorithm. This does not contradict our previous conclusion that there exist some isolated, compact objects which are not embedded in larger galaxies. What we are suggesting is that these correlations should be interpreted with care and that many intermediate and high redshift compact galaxies do not have close

companions nor extended flux surrounding them.

Numerical simulations have shown that the progenitors of a galaxy at $z = 0$ formed in a hierarchical clustering scenario would be detected at $z = 3$ as several protogalactic clumps covering an area on the sky the size of a WFPC2 chip or larger, and thus not highly correlated (Haehnelt, Steinmetz & Rauch 1996 [p. L96]; Rauch, Haehnelt & Steinmetz 1997; Steinmetz 1998). Our results are consistent with, but do not confirm, this picture.

This research was supported in part by NASA grant NAG 5-3042, which is gratefully acknowledged. We thank the anonymous referee for suggestions that improved the manuscript.

A. THE NATURE OF NIC118.0 = WFPC2 4–601.0

As discussed briefly in §2, the highest formal photometric redshift derived by TWS in their catalog is for the object NIC118.0 = WFPC2-601.0 at a redshift of 6.56.

For simplicity of notation we refer to the four wavebands F160W, F110W, F814W, and F606W as H_{160} , J_{110} , I_{814} , and V_{606} , though readers should note that the HST wavebands are not the standard Johnson filters, particularly the F110W. The associated color indices for our measured AB magnitudes in these four wavebands through an 0.6" aperture of 27.79, 27.68, 30.41 and 30.44 yield associated color indices of $J_{110} - H_{160} = -0.11$, $I_{814} - J_{110} = 2.73$, and $V_{606} - I_{814} = 0.03$. It is the latter two color indices which make the interpretation especially puzzling. Evidently, the precision of the I_{814} and V_{606} magnitudes and the associated color index is poor, though the agreement of our flux with that given in the WFPC-2 catalog (Williams *et al.* 1996) is fairly good. The significance of the V_{606} and I_{814} detections in our convolved images is only about 1σ but in the original WFPC2 images this object is detected with a 5.75σ significance. Visual inspection of the images makes it almost certain that there are positive detections in the V_{606} and I_{814} wavebands and that the V_{606} flux is not substantially less than the I_{814} flux. The original F606W and F814W WFPC2 images are shown in figure 11. Inspection and measurement of the profiles in the H_{160} and J_{110} images clearly show the object to be definitely non-stellar and somewhat irregular in appearance. It also appears to be extended in the I_{814} and V_{606} bands, though in these two bands the flux is so weak that we have not attempted to measure the profile. We therefore assume in the following that the object is extragalactic.

As noted in §2, though the fit has a fairly well defined minimum at the photometric redshift of 6.56, attenuation by Lyman absorption would be expected to produce a much larger $V_{606} - I_{814}$ index. To explore this further and to see whether a somewhat smaller redshift might be compatible with the above flux measurements we consider models for Lyman attenuation at 5 fiducial redshifts: 6.50, 6.25, 6.00, 5.75 and 5.50. Table A-1 shows the expected observed wavelengths of Lyman-alpha, Lyman-beta and the Lyman continuum for these 5 redshifts.

The recent discovery of very high redshift QSOs from the Sloan Survey (Fan *et al.* 2001) has allowed estimates of the Lyman attenuation to be extended beyond the range where the empirical estimates of Madau (1995), were made. Extrapolation of the Madau results were used in calculating the TWS photometric redshifts [Madau 1995 + detailed tables provided as private communication to R. Thompson)

In particular, Becker *et al.* (2001) have discussed the Lyman forest attenuation up to the highest redshift QSO which they discovered ($z = 6.28$). Their results show that the

region slightly shortward of the Lyman-alpha emission is black to within the errors of their measurements. They also set very low limits on the amount of flux transmitted below the Lyman-beta emission line, but there appears to be some flux between 7500-8000A, though one cannot be sure to what extent this represents sky subtraction errors.

Becker *et al.* model the expected flux at the Lyman-beta line by assuming that the Gunn Peterson trough optical depths at Lyman-alpha and Lyman-beta scale as the ratio of the f-values (actually they should scale as the ratio of the product of the wavelength and f-value), so in this simple model the ratio of the Gunn Peterson trough at Ly α to that at Ly beta (for a given redshift) should have a ratio of 6.24. This same modeling can be extended in a straightforward fashion to include the Lyman continuum attenuation. We refer to this simple Gunn Peterson model as the “uniform” model.

In fact, the empirically-derived ratio of the attenuation from Lyman-alpha to that associated with Lyman-beta (at a fixed absorption redshift, not a fixed observed wavelength) derived by Madau (1995) at somewhat lower redshifts yields effective optical depth ratios (Ly α /Ly β) which are substantially lower—of order 2.0.

The reason for this discrepancy must almost certainly be due to the lumpiness of the gas (“clouds”) which presumably persists to higher redshifts. We have therefore used, as an alternative to the “uniform” model above, a simple “picket-fence” model in which the Lyman-alpha optical depth varies over small regions of redshift space between a relatively small value (τ_{min}) and a large value (τ_{max}) with the large value covering a fraction, f, of a given redshift interval. The higher extinction in the τ_{max} component causes Lyman-beta to be saturated in the region of redshift space covered by this component. Unless sufficiently high SNR and high resolution observations are carried out, the measured transmission will be the average of the transmission associated with these two components. Additionally, if the high effective optical depth of the Lyman-beta transmission at very high redshifts estimated by Becker *et al.* (for example ~ 3), is interpreted in terms of the uniform model, it requires a Lyman-alpha optical depth of ~ 19 , which seems excessive given their published estimates, unless there is a truly abrupt and huge discontinuity in this quantity. We have therefore used combinations of τ_{min} , τ_{max} , and f whose properties are in reasonable accord with these high redshift QSO observations, but fixing them so that the effective ratio of Ly α to Ly β optical depths is around 2, in accordance with the Madau (1995) results. With the run of these three parameters as a function of redshift, the contribution from the higher Lyman lines and continuum is determined. This may or may not be in conflict with the limit on the Lyman-beta flux observed by Becker *et al.* at the highest redshifts. In this model, one of the three parameters above is free and we have arbitrarily fixed the thick component at an optical depth of 30.0.

We show the effective low resolution optical depths for both the uniform and picket fence models for an emission redshift of 6.0 in figure 12.

There is no difference in the two models in the region to the red of the Lyman-beta absorption, but to the blue of it, because of the rapid drop in the ratio of the Gunn-Peterson optical depths with increasing Lyman line number at a fixed redshift, the increasing number of Lyman lines capable of producing absorption does not compensate for the decrease in the Lyman-alpha optical depth with decreasing redshift. In the picket fence model, the opposite is true, since the drop in the effective opacity as one progresses to higher Lyman lines is much slower, and in fact the curve for the picket fence absorption resembles the empirical Madau curves for lower redshifts, as expected.

Even this picket fence model probably underestimates the actual attenuation shortward of the Lyman limit, since it is highly likely that much thicker clouds intervene. Measurements at lower redshifts (Giallongo *et al.* 2002) strongly suggest that almost no Lyman continuum radiation is escaping. However, it is conceivable that a very luminous burst of hot stars in a protogalaxy could produce its own proximity effect and allow some Lyman continuum radiation to escape.

To get the smallest V-I color in the face of the Lyman attenuation, we use a very hot model, namely a burst of star formation lasting just 25 mY and ending at the 5 fiducial redshifts, and with no internal or external dust reddening. Using these two simple models for the Lyman attenuation produces the results shown in table A-2.

Note that the progression in the V-I color index for the Uniform model is not monotonic with increasing emission line redshift because the reduction in the I-J color due to Lyman-alpha cutting into the I band reduces the I band flux relative to the more-or-less unaffected J-band flux more rapidly than the relatively weak Lyman continuum attenuation affects the V-band flux, (though the V-H index is monotonic). The strong attenuation in the Lyman continuum in the picket fence model causes the V-I color index to strongly rise with increasing redshift. In any case, it is clear that even the Uniform model cannot come close to reproducing the observed colors, and the (in our opinion more realistic) picket fence model fails even more badly.

In fact, the attempt to find a solution at very high redshifts without *any* Lyman attenuation fails: The reason is that the intrinsic Lyman continuum edge in even the very hot 25mY model in the intrinsic stellar population gives a V-I color index which is much too red, as shown in the last model “No Ly Abs”.

We conclude that if subsequent observations *do* establish the very high redshift nature of this object then it must have some extraordinary properties.

The alternative of a lower redshift object suffering from internal reddening is no more successful: A shallow secondary minimum in the χ^2 search for the best combination of redshift, internal reddening and population template occurs at a redshift of 0.2, while the tertiary minimum occurs at a redshift of 1.05. The resulting color indices for $z = 0.2$ are 1.36 and 1.22 for V-I and I-J respectively, while for $z = 1.05$ they are 1.22 and 1.16. Both of these sets of indices are very far from the observed values. The problem is obvious: An amount of reddening sufficient to produce a very red observed I-J index would also produce an even larger V-I index since the extinction increases with decreasing rest wavelength.

A.1. Superposition of Two Objects

It is conceivable that NIC118.0 is actually a superposition of two objects with very different redshifts. One would be a truly very high redshift object for which the Lyman attenuation can produce the large I-J color, with a low redshift, hot dwarf galaxy providing some of the V flux. Given the excellent positional agreement between the WFPC-2 and NIC-MOS images, together with the intrinsic very rare nature of such a very high redshift object (and moderately rare low redshift hot dwarf) such a solution seems to us quite artificial.

A.2. Concluding Comments

Although there are important differences, the dilemma posed by this object is reminiscent of that posed by the object HDF-N J123656.3+621322 (Dickinson *et al.* 2000), which has strong flux in K_s and H, but no convincing detection in any of the shorter wavebands. Its nature is still (as far as we are aware) uncertain, but these authors raise the possibility (among others) of an AGN, with emission lines possibly influencing the colors. Without further observations of NIC118.0, however, further speculation seems fruitless.

An attempt is being made by Spinrad *et al.* to obtain spectra of this object, but the results are inconclusive so far.

The GOODS HST Treasury program will, unfortunately, probably not go deep enough in V or I to detect this object, but the new Z-band observations may add an important clue. It may be up to either NGST or the next generation of very large ground based telescopes to reveal its nature.

REFERENCES

- Becker, R.H., Fan, X., White, R.L., Strauss, M.A., Narayanan, V.K., Lupton, R.H., Gunn, J.E., Annis, J., Bahcall, N.A., Brinkmann, J., Connolly, A.J., Csabai, I., Czarapata, P.C., Doi, M., Heckman, T.M., Hennessy, G.S., Ivezić, Z., Knapp, G.R., Lamb, D.Q., McKay, T.A., Munn, J.A., Nash, T., Nichol, R., Pier, J.R., Richards, G.T., Schneider, D.P., Stoughton, C., Szalay, A.S., Thakar, A.R., York, D.G. 2001, *AJ*, 122, 2850
- Bertin, E., and Arnouts, S. 1996, *A&A*, 117, 393
- Colley, W.N., Rhoads, J.E., Ostriker, J.P., & Spergel, D.N. 1996, *ApJ*, 473, L63
- Cohen, J.G., Hogg, D.W., Blandford, R., Cowie, L.L., Hu, E., Songaila, A., Shopbell, P., and Richbert, K. 2000, *ApJ*, 538, 29
- Dickinson, M. 1998, in proceedings of ‘Space Telescope Science Institute Symposium: The Hubble Deep Field,’ eds. Livio, M., Fall, S.M., Madau, P. (Cambridge University Press:New York), 219
- Dickinson, M., Hanley, C., Elston, R., Eisenhardt, P.R., Stanford, S.A., Adelberger, K.L., Shapley, A., Steidel, C.C., Papovich, C., Szalay, A.S., Bershady, M.A., Conselice, C.J., Ferguson, H.C., Fruchter, A.S. 2000 *ApJ*, 531, 624
- Efstathiou, G., Bernstein, G., Katz, N., Tyson, J.A., Guhathakura, P. 1991, *ApJ*, 380, L47
- Fan, X., Narayanan, V.K., Lupton, R.H., Strauss, M.A., Knapp, G.R., Becker, R.H., White, R.L., Pentericci, L., Leggett, S.K., Haiman, Z., Gunn, J.E., Ivezić, Z., Schneider, D.P., Anderson, S.F., Brinkmann, J., Bahcall, N.A., Connolly, A.J., Csabai, I., Doi, M., Fukugita, M., Geballe, T., Grebel, E.K., Harbeck, D., Hennessy, G., Lamb, D.Q., Miknaitis, G., Munn, J.A., Nichol, R., Okamura, S., Pier, J.R., Prada, F., Richards, G.T., Szalay, A., York, D.G. 2001, *AJ*, 122, 2833
- Ferguson, H.C. 1998, in proceedings of ‘Space Telescope Science Institute Symposium: The Hubble Deep Field,’ eds. Livio, M., Fall, S.M., Madau, P. (Cambridge University Press:New York), 181
- Fernandez-Soto, A., Lanzetta, K.M., Yahil, A. 1999, *ApJ*, 513, 34
- Giallongo, E., Cristiani, S., D’Odorico, S., Fontana, A. 2002, *ApJ*, 568, L9
- Haehnelt, M., Steinmetz, M. & Rauch, M. 1996, *ApJ*, 465, L95
- Madau, P. 1995, *ApJ*, 441, 18

- O’Connell, R.W., and Marcum, P. 1997, in proceedings of ‘The Hubble Space Telescope and the High Redshift Universe,’ eds. Tanvir, N.R., Aragón-Salamanca, A., & Wall, J.V., (World Scientific:London) 63
- Rauch, M., Haehnelt, M. & Steinmetz, M. 1997, ApJ, 481, 601
- Roche, N., Shanks, T., Metcalfe, N., Fong, R. 1996, MNRAS, 280, 397
- Steidel, C.C., Giavalisco, M., Dickinson, M., Adelberger, K.L., 1996, AJ, 112, 352
- Steinmetz, M. 1998, in proceedings of ‘Space Telescope Science Institute Symposium: The Hubble Deep Field,’ eds. Livio, M., Fall, S.M., Madau, P. (Cambridge University Press:New York), 168
- Szalay, A.J., Connolly, A.J., and Szokoly, G.P. 199, AJ, 117, 68
- Thompson, R.I., Storrie-Lombardi, L.J., Weymann, R.J., Rieke, M.J, Schneider, G., Stobie, E. & Lytle, D. 1998, AJ, 117, 17
- Thompson, R.I., Weymann, R.J., and Storrie-Lombardi, L.J. 2001, ApJ, 546, 694
- Weymann, Ray, J., Stern, D., Bunker, A., Spinrad, H., Chaffee, F.H., Thompson, R.I., and Storrie-Lombardi, L.J., 1998, ApJ, 505, L95.
- Williams, R.E., Blacker, B. Dickinson, M., Dixon, W.V.D, Ferguson, H.C., Fruchter, A.S., Giavalisco, M., Gilliland, R.L., Heyer, I. Katsanis, R., Levay, Z. Lucas, R.A., McElroy, D.B., Petro, L., Postman, M., Adorf, H-M., and Hook, R.N. 1996, AJ, 112, 1335.

Table 1. High Redshift Candidates

(1) NICMOS ID ^a	(2) WFPC2 ID ^b	(3) AB (F160W) Total	(4) 0.6" ap.	(5) RA +12h36m	(6) Dec +62d	(7) z_{phot} (best)	(8) Robust Flag	(9) z_{phot} (5%)	(10) z_{phot} (90%)	(11) Rank
131.000	4-530.0	27.5	27.8	45.15	11:59.7	4.56	R	4.32	4.64	3
1081.00	4-748.0	28.3	28.4	41.96	12:09.1	4.64	NR	0.48	4.88	13
287.000	4-148.0	27.9	28.6	48.92	12:16.7	4.64	NR	0.48	4.80	11
1075.00	4-526.0	28.6	28.8	45.11	12:00.4	4.72	NR	0.48	4.88	29
274.000	4-200.0	26.0	26.5	48.37	12:17.3	4.72	R	4.48	4.80	2
267.000	4-314.0	27.3	27.5	48.00	12:00.8	4.80	R	4.64	4.80	1
150.000	...	26.9	27.5	45.42	12:02.2	4.80	R	4.56	5.04	1
96.0000	...	27.4	27.9	44.54	12:36.1	4.88	NR	0.96	5.44	11
693.000	...	28.2	28.6	48.86	12:16.8	4.88	NR	0.96	5.12	12
92.0000	4-499.0	27.4	27.7	44.44	12:17.2	4.88	NR	0.96	5.52	30
562.000	4-663.0	28.8	28.9	43.91	11:54.4	4.88	NR	0.96	5.20	16
277.212	4-169.0	24.6	25.1	48.71	12:16.7	5.04	R	4.80	5.12	1
1040.00	...	28.1	28.7	47.83	12:04.5	5.44	NR	0.00	5.76	17
184.000	4-473.0	26.6	26.9	45.88	11:58.2	5.52	SC	5.20	5.52	1
645.000	4-262.2	28.1	28.2	46.45	12:37.5	5.52	R	4.88	5.76	2
586.000	...	27.5	28.0	44.71	12:20.0	5.68	R	4.80	6.00	1
248.000	...	27.2	27.7	47.46	11:59.9	5.76	NR	0.08	6.00	19
107.000	...	27.1	27.7	44.72	12:18.8	5.92	R	4.80	6.32	2
118.000	4-601.0	27.5	27.7	44.90	11:50.3	6.56	NR	0.24	6.88	20

References. — (a) Thompson, Weymann, & Storrie-Lombardi 2001; (b) Williams *et al.* 1996

Table 2. F814W - F160W Colors for Averaged Galaxies

Galaxy	Filter	Photometry Aperture			
		Isophotal	0.6''	1.5''	2.5''
F300W dropout	F814W	28.3	28.5	28.3	28.5
	F160W	27.6	27.9	27.6	27.7
	F814W - F160W	0.7	0.6	0.7	0.8
F450W dropout	F814W	28.5	28.6	28.7	29.0
	F160W	28.4	28.5	28.8	28.7
	F814W - F160W	0.1	0.1	-0.1	-0.3

Note. — The apertures sizes listed are diameters. The calculated errors for the photometry are of order ± 0.1 . It can be seen from the table that the uncertainties are at least this large as the 2.5'' aperture gives a slightly fainter magnitude than the 1.5'' aperture for the F160W filter.

Table 3. Mass Limits

Case	z=2.7		z=3.9	
	F300W dropouts		F450W dropouts	
	M_{\odot}	$M_{\odot}yr^{-1}$	M_{\odot}	$M_{\odot}yr^{-1}$
i	3.9e8	...	1.1e9	...
ii	1.5e8	...	1.8e8	...
iii	1.8e7	0.36	6.1e7	1.3

Table A-1. Expected Observed Wavelengths [\AA]

	Emission Redshift				
	6.50	6.25	6.00	5.75	5.50
Ly α	9117	8814	8510	8206	7902
Ly β	7693	7436	7180	6924	6667
Ly-limit	6838	6610	6382	6154	5926

Table A-2. Predicted Colors

Model	Emission Redshift									
	5.5		5.75		6.0		6.25		6.5	
	V-I	I-J	V-I	I-J	V-I	I-J	V-I	I-J	V-I	I-J
Uniform	1.53	0.47	1.63	0.76	1.75	1.09	1.75	1.53	1.62	2.12
Picket Fence	2.41	0.47	3.02	0.76	4.35	1.11	5.50	1.63	6.81	2.31
No Ly Abs	0.71	-0.34	0.89	-0.28	1.09	-0.23	1.29	-0.18	1.47	-0.11

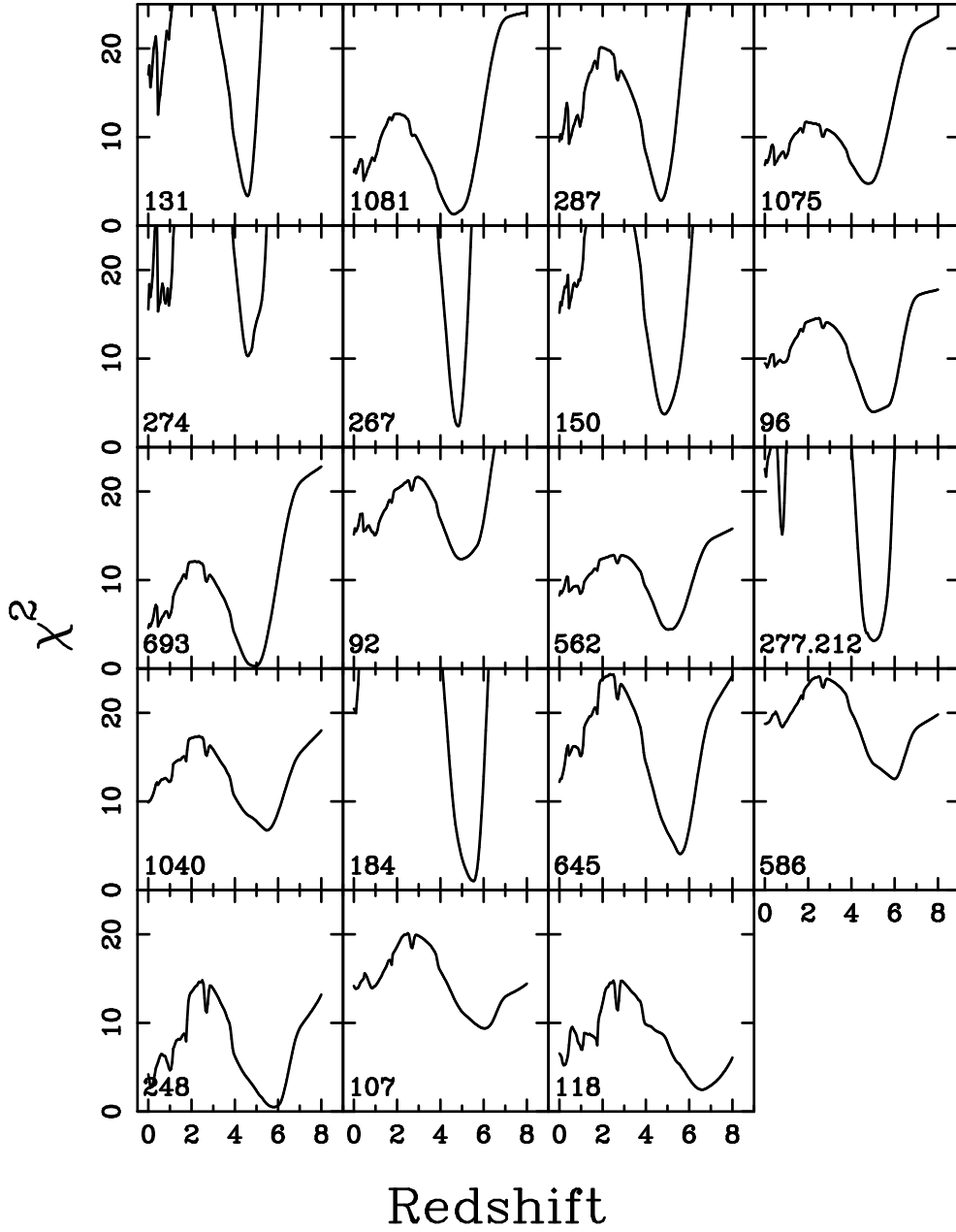


Fig. 1.— The variation of the χ^2 parameter versus redshift for the 19 high redshift candidates. The numbers in each panel refer to the NICMOS identification in the TWS catalog.

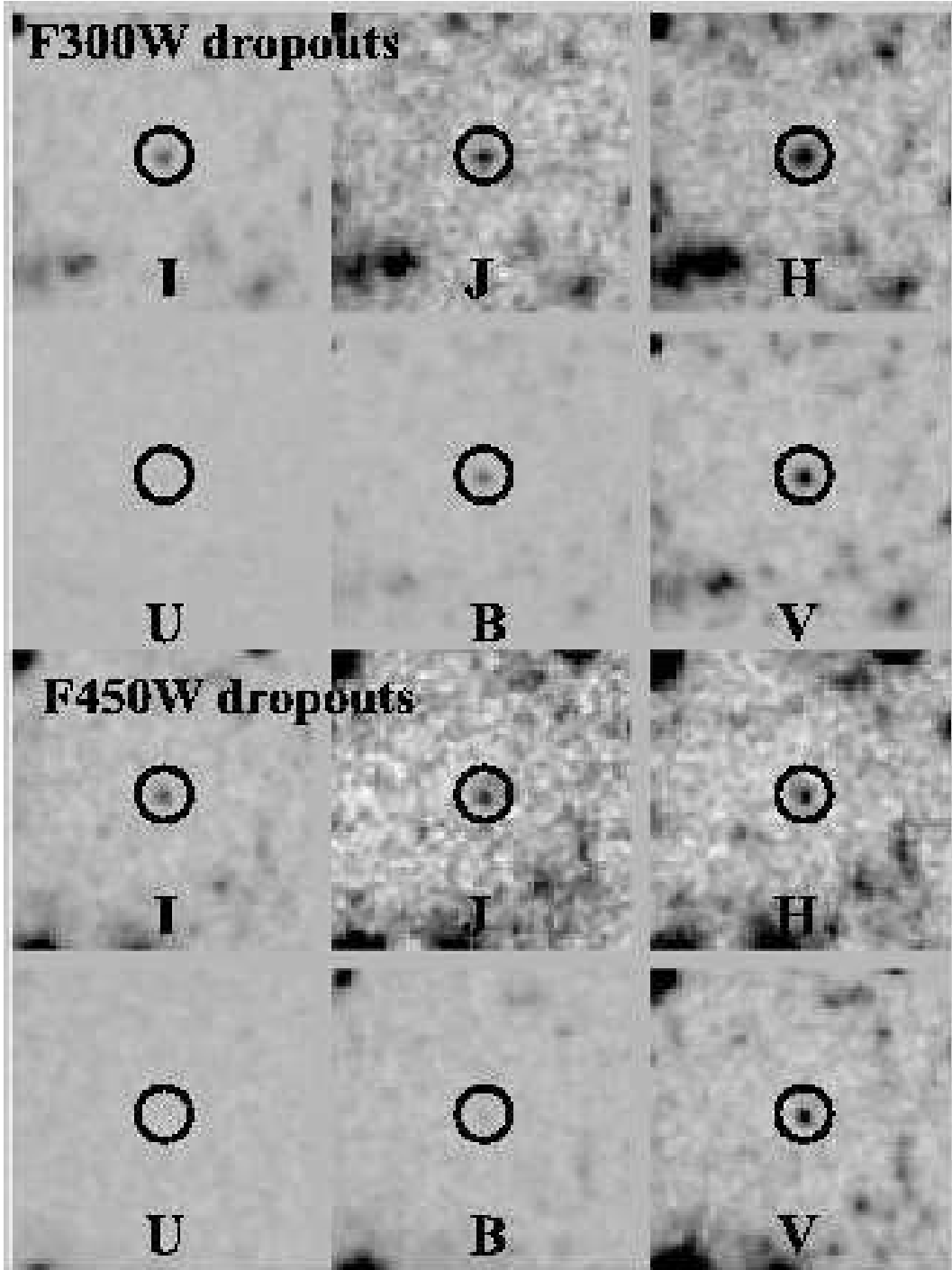


Fig. 2.— The averaged isolated F300W and F450W dropout galaxies are shown in the 6 HST wavebands. The estimated photometric redshifts are $z = 2.70$ and $z = 3.9$, respectively. The frames are 6.0 arcseconds on a side and the averaged galaxies are overlaid with 1.0 arcsecond diameter apertures.

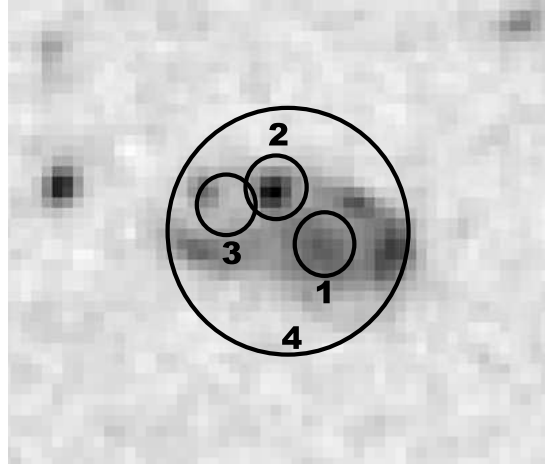


Fig. 3.— The WFPC2 combined F606W+F814W image of WFPC2 4–378.0 whose redshift is $z = 1.225$ is shown. The frame has been resampled to match the orientation and resolution of the NICMOS images. The four apertures refer to: 1=bright F160W nucleus, 2=bright F814W off-nuclear knot, 3=dim F814W off-nuclear region, and 4=the whole galaxy. The flux was measured in $0.6''$ diameter apertures for positions 1 through 3 and a $2.6''$ aperture for position 4. The photometric redshifts for each of these apertures were $z = 1.20$ or $z = 1.25$.

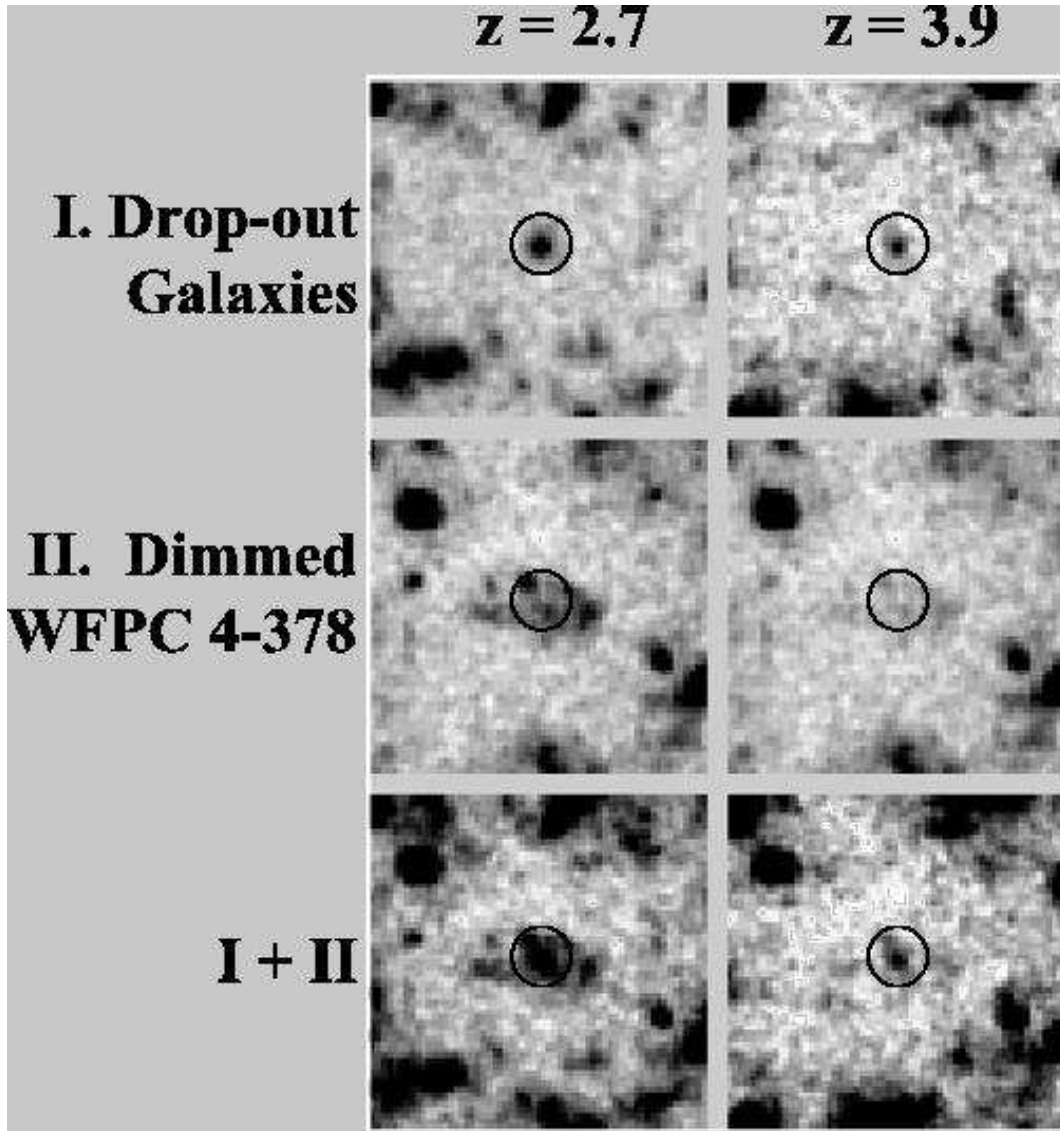


Fig. 4.— The figure simulates what a star-forming galaxy like WFPC2 4–378 would look like in the F160W filter if it were redshifted to $z = 2.7$ (left panels) and $z = 3.9$ (right panels). The top panels (I) reproduce the F300W and F450W dropout galaxies in the F160W band. The middle panels (II) show the F606W image appropriately dimmed and scaled as it would approximately appear in the F160W band at these redshifts, while the bottom panels (I+II) show the addition of the top and middle panels. Comparison of the top and bottom panels show that the F300W and F450W drop averaged images lack the extended flux which an active star-forming galaxy like WFPC2 4–378 shows. The images are 6 arcseconds on a side and a 1 arcsecond diameter aperture is overlaid on each image.

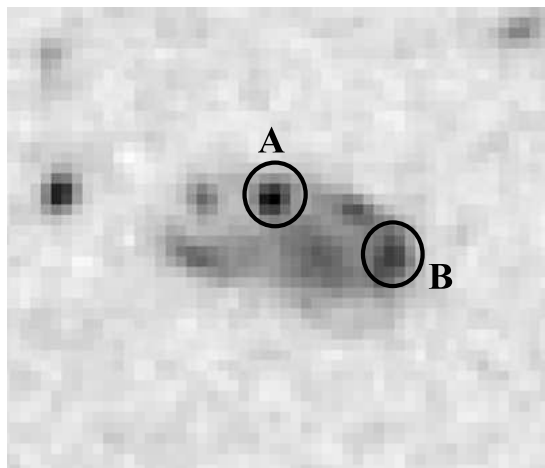


Fig. 5.— This is the same image of WFPC2 4–378.0 as shown in figure 5. The two bright star-forming knots used as centers of rotation for the simulations are marked as A and B.

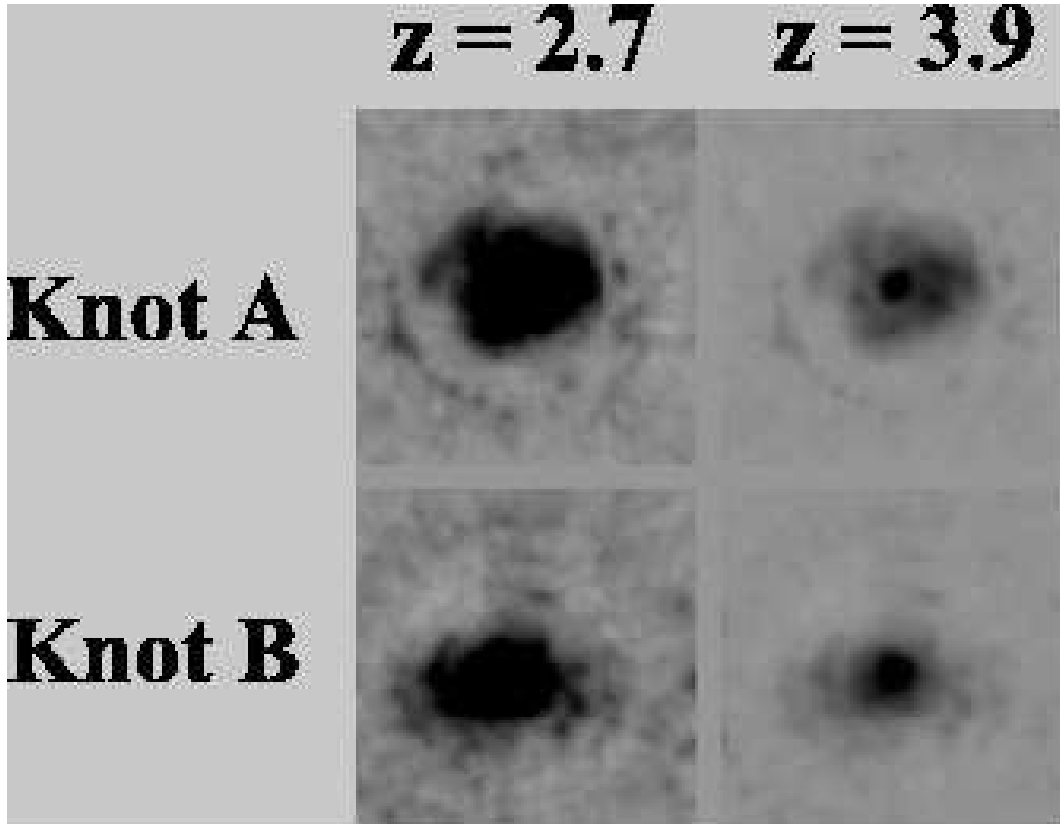


Fig. 6.— The expected appearance of WFPC2 4–378 through the F160W bandpass at redshifts of $z = 2.7$ (on the left) and $z = 3.9$ (on the right) after summing 20 random rotations about star-forming knots A (top row) and B (bottom row). The extended structure is readily apparent, in contrast to the F300W and F450W dropout F160W images in figure 2. The images are 6 arcseconds on a side.

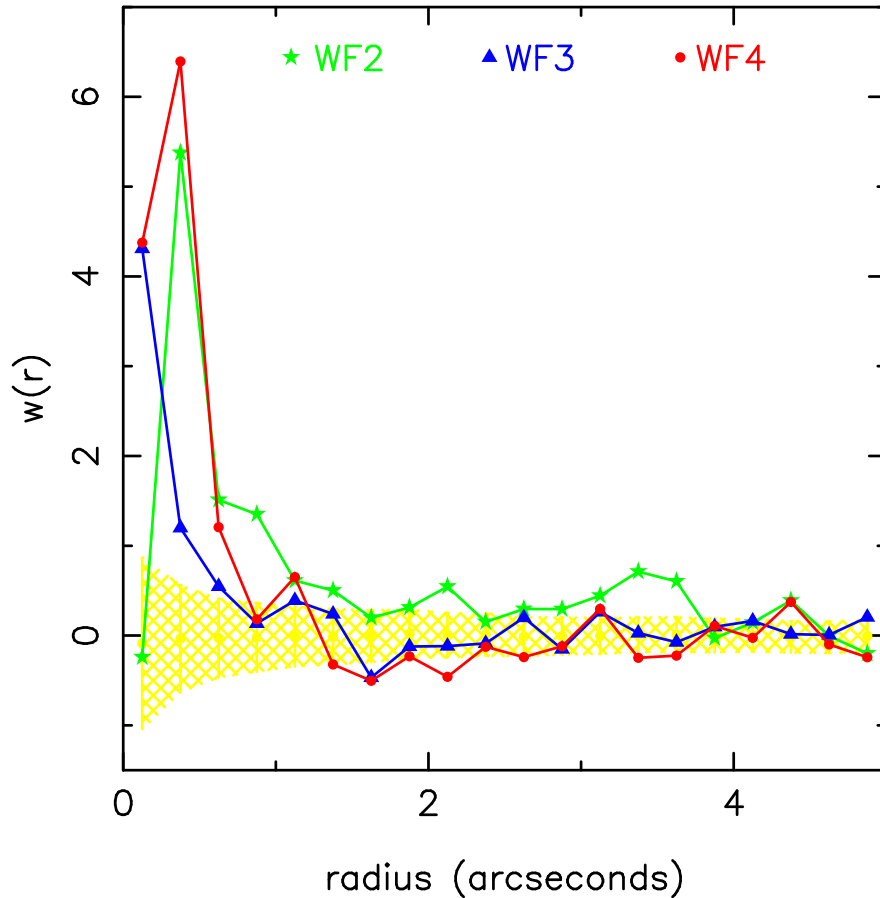


Fig. 7.— The angular correlation function for the high redshift color sample of WFPC2 HDF north observations in chips 2, 3, and 4, are marked with stars, triangles, and circles, respectively. The $\pm 1\sigma$ range for no correlation, determined from 500 realizations of randomly placed points, is shown as the crosshatched region around $w(r) = 0$. There is a strong signal for all three WFPC2 chips on scales $r < 0.5''$, confirming the result found by (Colley *et al.* 1996). The signal is significant at the $3 - 7\sigma$ level, and peaks at $0.25'' - 0.5''$.

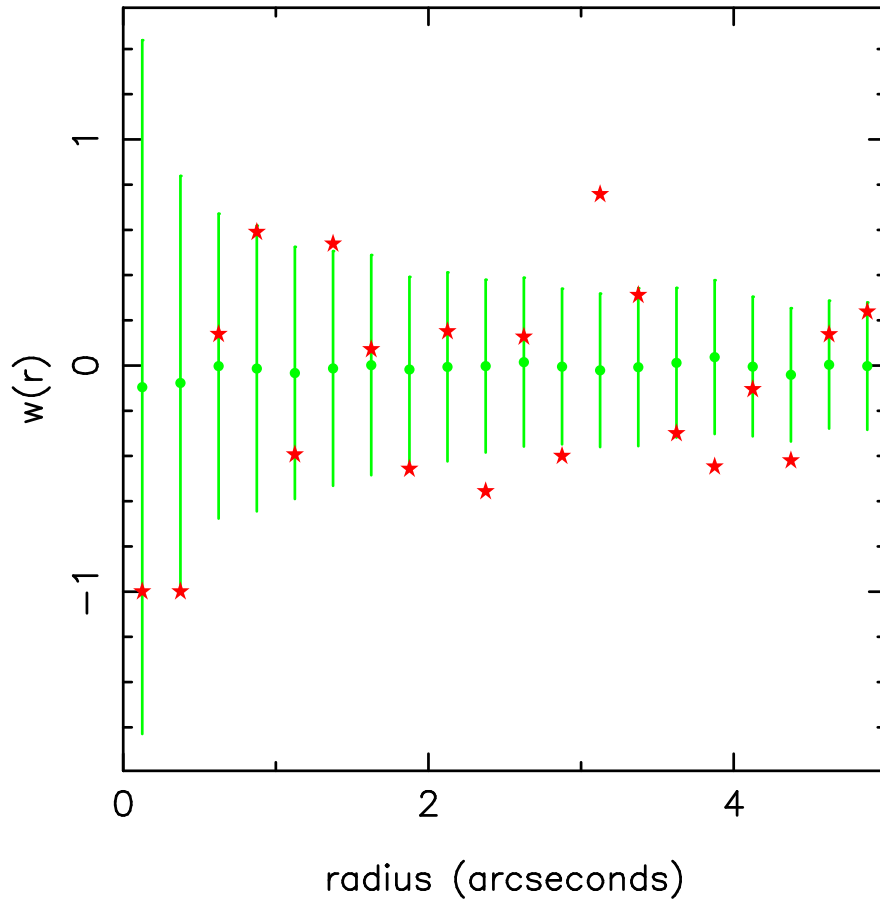


Fig. 8.— The autocorrelation signal for the catalog of the 93 small galaxies from the NICMOS data set. The data is marked with stars, the mean in each bin for the random simulations is marked with solid circles, and the error bars are $\pm 1\sigma$ determined from the simulations. No correlation signal is seen, in contrast to the signal detected in the WFPC2 data set shown in figure 7.

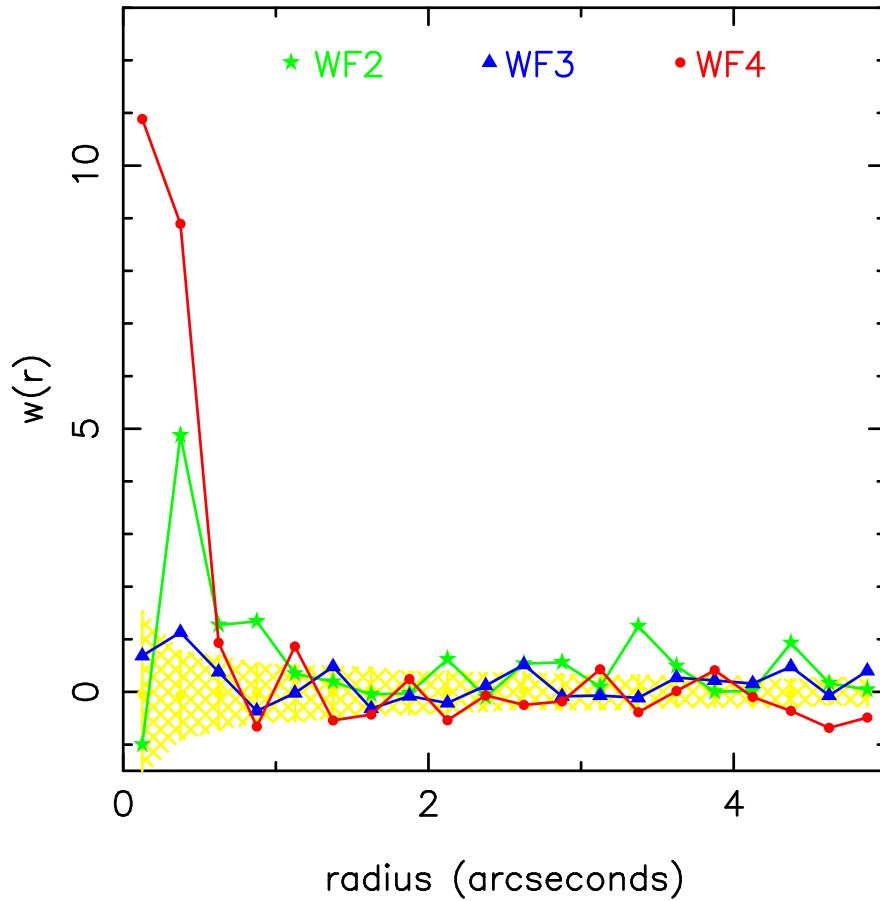


Fig. 9.— The autocorrelation function for the same sample as that shown in figure 7 but now restricted to $0.65''$ regions, to match the size of the NICMOS field. The symbols are as in figure 7. The signal in chip 4 is actually stronger in the smaller field compared to the full WFPC2 field, about the same in chip 3, and smaller in chip 2.

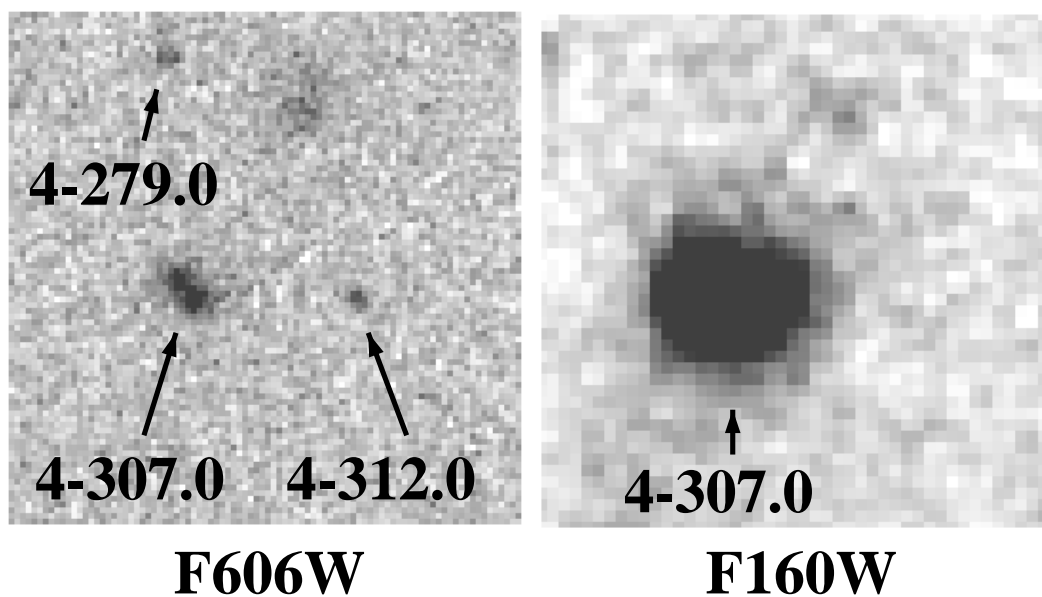


Fig. 10.— The F606W and F160W images of a $4.5'' \times 4.5''$ region of the northern Hubble Deep Field. The galaxy just left of the center in both images is WFPC2 4–307.0 (NIC166.000). WFPC2 4–312.0 is the galaxy $1.5''$ to the right of 4–307.0 and WFPC2 4–279.0 is the galaxy $2.1''$ above 4–307.0 in the F606W image. We measure $0.6''$ F606W aperture AB magnitudes of 29.4 and 28.6 for WFPC2 4–312.0 and 4–279.0, respectively. These objects are not formally detected by SExtractor in the F160W image for the S/N thresholds we have adopted, however they have measured F160W $0.6''$ aperture magnitudes of 29.7 and 29.6 at the positions corresponding to the F606W centroids. By contrast, WFPC2 4–307.0 has $0.6''$ aperture magnitudes in F606W and F160W of = 27.2 and 23.0.

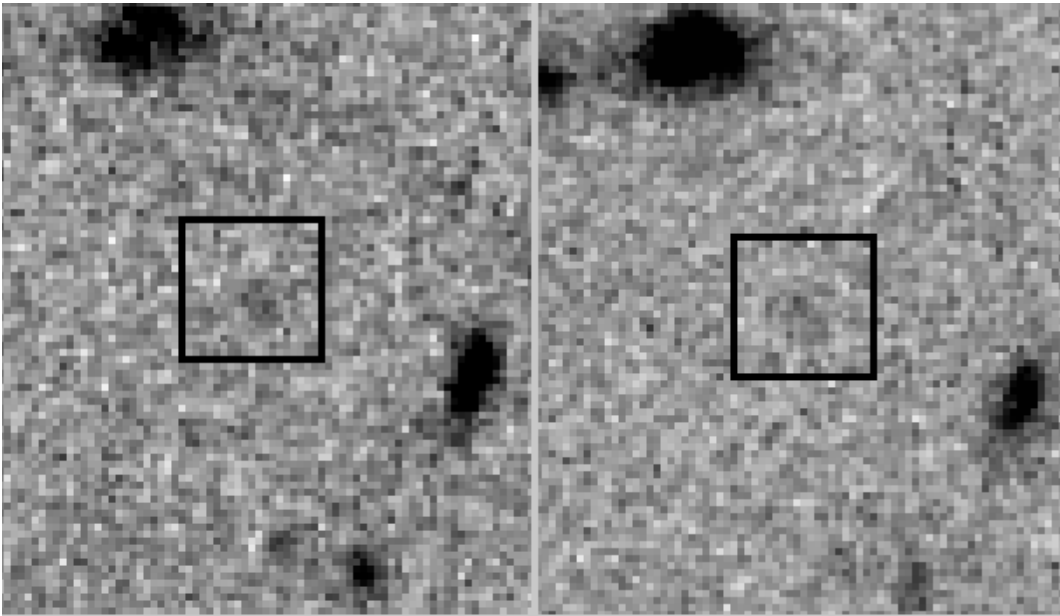


Fig. 11.— The WFPC2 images for HDF 4-601.0 (NIC118.0) in the F606W (left) and F814W (right) filters are shown. This object is detected at a 5.75σ significance with isophotal AB magnitudes of F814W=30.0 and F606W=30.5 (Williams *et al.* 1996). Though faint, there is clearly flux detected in both wavebands which makes a redshift of $z = 6.6$ for this object problematic. There is a 1 arcsecond box centered on the object.

"Uniform" vs. "Picket-Fence" Model for $Z_{em} = 6.0$

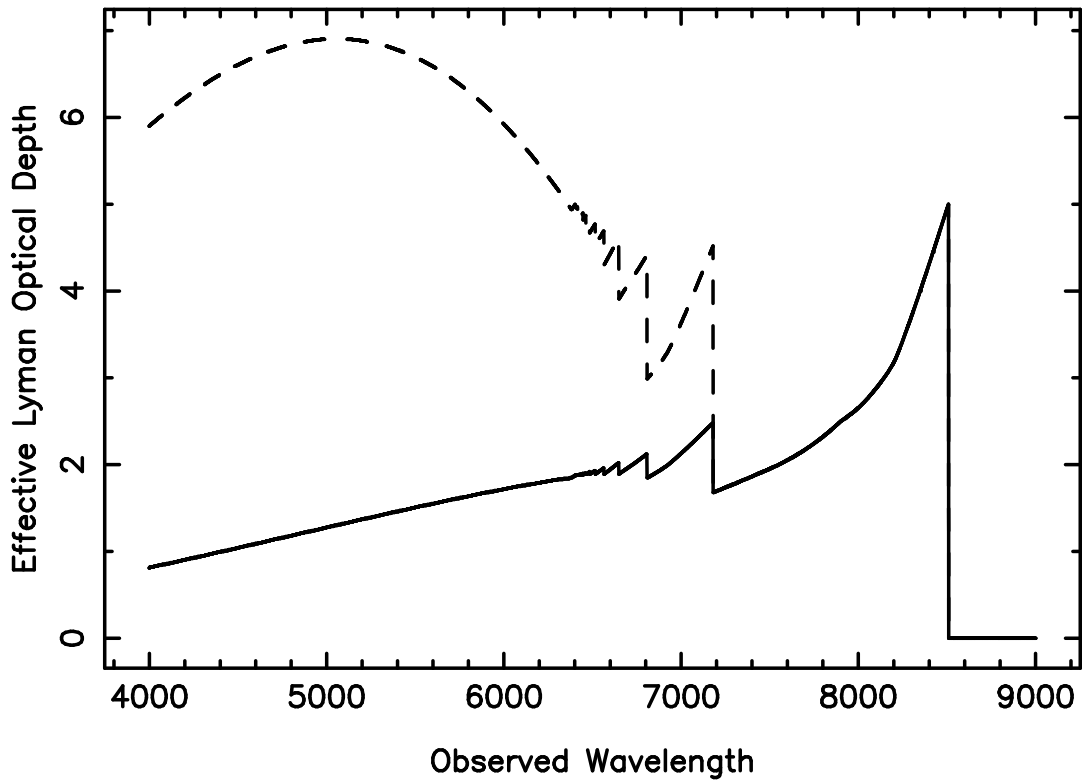


Fig. 12.— The effective optical depth versus wavelength for an emission redshift of $z=6$ for two models is shown. The solid line is for the “uniform” model and the dashed line is for the “picket fence” model. There is no difference in the models in the region redward of the $\text{Ly}\beta$ absorption (7175\AA) but they vary substantially in the blueward region.